Geothermics 54 (2015) 122–135

Contents lists available at ScienceDirect

Geothermics

journal homepage: www.elsevier.com/locate/geothermics

# Mineral precipitation during production of geothermal fluid from a Permian Rotliegend reservoir

Simona Regenspurg[a,*], Elvira Feldbusch[a,1], James Byrne[b,2], Firorenza Deon[a,3], Dejene Legesse Driba[a,4], Jan Henninges[a,1], Andreas Kappler[b,5], Rudolf Naumann[a,6], Thomas Reinsch[a,7], Christine Schubert[a,8]

[a] Helmholtz Centre Potsdam, German Research Centre for Geosciences, Telegrafenberg, D-14473 Potsdam, Germany
[b] University of Tübingen, Centre for Applied Geosciences, Germany

ARTICLE INFO

*Article history:*
Received 5 August 2014
Accepted 10 January 2015

*Keywords:*
Scaling
Native copper
Laurionite
Magnetite
Rotliegend formation
Mössbauer spectroscopy
Geothermal fluid

ABSTRACT

Highly saline geothermal fluids typically contain a complex mixture of metals that are responsible for precipitation of various minerals during the operation of geothermal plants. This has resulted in significant clogging of the production well at the geothermal site Groß Schönebeck (Germany).

A large number of different sample types have been collected from this site including solid precipitates from filters above ground, directly from the borehole fill, and from the material flushed out by various well cleaning operations. The sampled material filling the well is predominantly composed of native copper ($Cu^0$), barite ($BaSO_4$), magnetite ($Fe_3O_4$), and lead (Pb) bearing phases such as laurionite (PbOHCl), as well as minor amounts of calcite ($CaCO_3$), and an amorphous phase containing mainly Si, Fe, Ca, Pb, and Al.

While some minerals such as barite precipitate due to oversaturation upon cooling, the formation of native copper requires a redox reaction, that can be induced by reduction of Cu(I) or Cu(II) by elemental iron ($Fe^0$). Results from this study indicate that highly concentrated Cu and Pb containing fluids are characteristic for the host rock, which is Permian Rotliegend sandstone with an underlying Permo-Carboniferous volcanic rock. Due to the high salinity of the formation fluids, heavy metals can be enriched in these waters by formation of aqueous metal chloride complexes. When this fluid comes in contact with the $Fe^0$ of the carbon steel liner, the Cu is immediately reduced and precipitation occurs. As further corrosion products, magnetite ($Fe_3O_4$) and (X-ray amorphous) Fe(II) phases have been identified by Mössbauer spectroscopy. The formation of the mineral laurionite consumes both Pb and hydroxide ions. Thus, its precipitation decreases the pH-value resulting in a proton excess which is most likely consumed by calcite dissolution, resulting in buffering the pH to around neutral.

The clogging process of the well is accelerated by frequently alternating periods of fluid production and shut-in providing repeatedly "fresh" (metal-rich) reservoir fluid which subsequently reacts with the casing or oversaturates upon cooling.



## 1. Introduction

The exploitation of geothermal energy in areas of average geothermal gradients is a promising future alternative for heat and electricity generation (Huenges, 2010). Reservoir rocks of high permeability, such as sandstones found in deep sedimentary basins are considered to be appropriate for drilling geothermal wells. Fluids in these aquifers at depths of several kilometers typically have high salinity of up to several hundred g/L (Kharaka et al., 1987; Hanor, 1994; Kharaka and Hanor, 2004). In the North German Basin, predominantly Triassic sandstone reservoirs have been exploited for geothermal energy (e.g. at the sites Neustadt-Glewe or Hanover-Horstberg; Seibt et al., 2005; Kehrer et al., 2007). At the geothermal in situ laboratory Groß Schönebeck (GrSk), however, Lower

* Corresponding author. Tel.: +49 331 288 1437; fax: +49 331 288 1437 1450.
*E-mail addresses:* regens@gfz-potsdam.de (S. Regenspurg), elkin@gfz-potsdam.de (E. Feldbusch), james.byrne@uni-tuebingen.de (J. Byrne), fdeon@gfz-potsdam.de (F. Deon), driba@gfz-potsdam.de (D.L. Driba), janhen@gfz-potsdam.de (J. Henninges), andreas.kappler@uni-tuebingen.de (A. Kappler), rudolf.naumann@gfz-potsdam.de (R. Naumann), reinsch@gfz-potsdam.de (T. Reinsch), Christine.schubert@gfz-potsdam.de (C. Schubert).
[1] Tel.: +49 331 288 1442; fax: +49 331 288 1437 1450.
[2] Tel.: +49 7071 29 74690; fax: +49 7071 29 5059.
[3] Tel.: +49 331 288 28714; fax: +49 331 288 1437 1450.
[4] Tel.: +49 331 288 1576; fax: +49 331 288 1437 1450.
[5] Tel.: +49 7071 29 74992; fax: +49 7071 29 5059.
[6] Tel.: +49 331 288 1426; fax: +49 331 288 1437 1474.
[7] Tel.: +49 331 288 1834; fax: +49 331 288 1437 1450.
[8] Tel.: +49 331 288 1437; fax: +49 331 288 1437 1450.

http://dx.doi.org/10.1016/j.geothermics.2015.01.003
0375-6505/

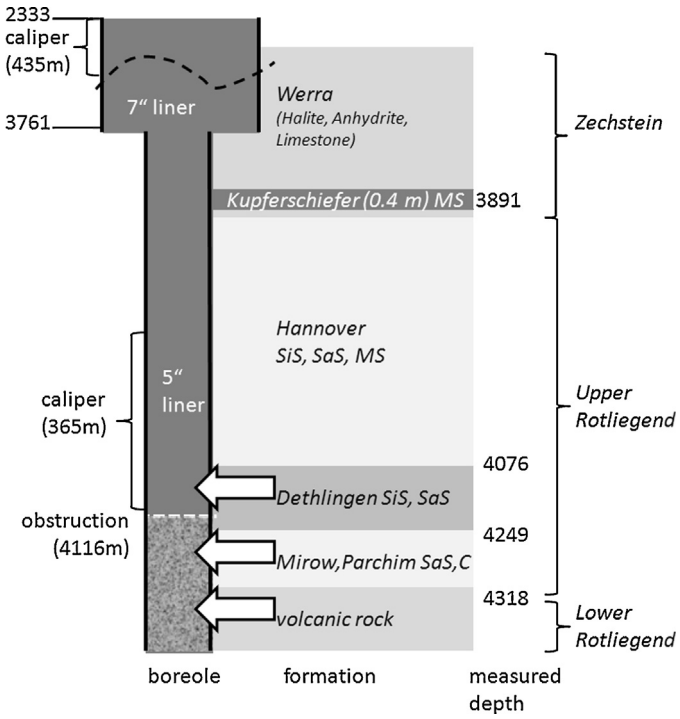


**Fig. 1.** Scheme of the Groß Schönebeck production well borehole completion, lithostratigraphic geological formations, maximum depth of the borehole fill (obstruction), and areas of caliper measurements. White arrows: stimulated sections; SiS: siltstone, SaS: sandstone, MS: mudstone, C: conglomerate. Clastic sediments are usually alternating sequences of silt, mud, coarse-, and fine sandstone.

Permian (Rotliegend) sandstones and the underlying volcanic rock formations are being investigated for geothermal applications. They were encountered in 1990 during gas exploration and comprehensive research on enhanced geothermal systems (EGS) has been carried out since 2001 (Huenges et al., 2006; Zimmermann et al., 2010). A geothermal well doublet system with a production (Gt GrSk 4/05) and an injection well (E GrSk 03/90) has been established. The reservoir is between 4100 m and 4300 m (true vertical) depth and consists of clastic sedimentary rocks of the Upper Rotliegend Dethlingen- and Mirow/Parchim formations underlain by Lower Rotliegend volcanic rocks that have been hydraulically stimulated by water- and gel-proppant fracs (Zimmermann et al., 2010; Fig. 1). The production well is deviated within the reservoir interval by 46–49° at maximum resulting in a horizontal distance of about 450 m between the wells in the reservoir (Zimmermann and Reinicke, 2010). Consequently, the total measured depth of the production well is of longer distance (4400 m) than its true vertical depth (4264 m). Reservoir engineering was successfully terminated in 2009 and first circulation tests (production of fluid and immediate re-injection) started in 2011. Samples of deep wellbore fluids have been analyzed both, before and after reservoir stimulation and classified as Na–Ca–Cl brine of very high salinity (265 g/L) and a gas to liquid volume ratio of about 1:1 with mainly $N_2$ (85–90%) and $CH_4$ (10–15%) in the gas phase (Wolfgramm et al., 2003; Regenspurg et al., 2010). These fluids are very characteristic for Rotliegend formations (Lüders et al., 2010) representing a complex elemental mixture including compounds that are considered to have strong scaling or corrosion potentials. Chloride ($Cl^-$) concentration amounts to nearly five molar thus being not only highly corrosive for carbon steel (e.g. Li and Ma, 2009) but also representing a strong complexing agent for many metals such as lead (Pb), iron (Fe) or zinc (Zn) which occur in concentrations between 100 and 200 mg/L in the GrSk fluids. Barium concentration is typically around saturation depending on temperature of the sampled fluid (Regenspurg et al., 2010). During fluid production tests, the accessible depth of the production well decreased by nearly 250 m (Fig. 2; Reinsch et al., in press), which can be linked to clogging by filling the well with precipitates (scaling).

The aim of this study is to identify (I) these scaling components of the fill as well as (II) the underlying chemical reactions responsible for their precipitation, and (III) to link these mineral precipitation reactions with the geological setting and fluid production operations in the well. This understanding is of importance not only for preventing further scale formation at the GrSk site or at geothermal wells in similar geological settings but also for understanding geochemical interactions at highly saline geothermal conditions.

## 2. Materials and methods

### 2.1. Activities at the Groß Schönebeck site since completion of the geothermal fluid loop

A summary of the main activities and sampling operations since April 2011 at the GrSk site is given in Table 1. Briefly, the fluid loop was established in spring 2011 (Frick et al., 2011). Subsequently, a series of circulation tests were carried out. Above ground a pressure of approximately 10 bar was maintained in the system to keep $CO_2$, a minor gas component (<1 vol %) in solution and to prevent atmospheric oxygen ($O_2$) from entering the fluid. Other fluid gases (mainly nitrogen and some methane) were separated from the fluid loop above ground and released into the atmosphere. After degassing, the fluid passed through some filter units (1–2 μm and 10–20 μm) before being re-injected into the reservoir. The fluid temperature at reservoir conditions was nearly 150 °C (Henninges et al., 2012), but due to relatively low flow rates (<20 $m^3$/h) and frequent shut-in periods (Fig. 2), the well head temperature was around 100 °C at maximum. At the end of the testing phase (April 2012), the accessible depth of the well had decreased from 4358 m to 4204 m (Fig. 2).

To find out the cause for this obstruction, solid samples with a volume of 0.5–2 L were retrieved from the depth of the well using a drive-down bailer (outer diameter: 45 mm) that penetrates ~0.5 m into the obstruction. After obtaining three samples from the production well and one from the injection well (end of July 2012), a short production test was carried out. Afterwards, a further decrease of the total depth was determined (4112 m; Fig. 1) and another bailer sample was collected (Table 1). To eventually remove the fill, a coiled tubing (CT) was inserted into the borehole to flush out the solid material by reverse circulation. This removed about 70 L to a depth of 4157 m (Reinsch et al., in press).

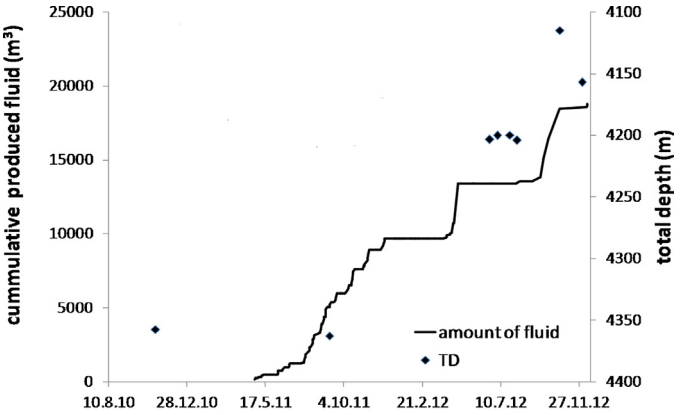


**Fig. 2.** Plot of the cumulative fluid that was produced and total depth over time in the Groß Schönebeck production well.

**Table 1**
Wellbore activities and sampling since April 2011 in the GrSk production (GrSk04) well.

| Date | Activities | Sample name | Sample type abbreviation |
|---|---|---|---|
| 04.2011–06.2012 | Several production-tests; determination of TD | Collection of fluid (wellhead) and filter residue samples (FR1-FR114) | WH-Fl, FR |
| 26.07.2012 | Drive down bailer | Three bailer samples (B115, 116, 117) from 4200 m (GrSk04) | B |
| 7.8.–8.8. 2012 | Short production tests (~7 h; 198 $m^3$) | – | |
| 8.8.2012 | Drive down bailer and TD | Bailer sample of GrSk04 (B119) | B |
| 30.112012–3.12.2012 | Coiled tubing operation | 33 samples (back flushing suspension) + three sediment container samples | CT |
| 10.12.–12.12.2012 | Production test (332 $m^3$) | Well head fluid and filter residue samples | WH-Fl, FR |
| 21.12.2012 | Drive down bailer and TD | Bailer sample of GrSk04 (134), 4162 m | B |
| 27.12.2012 | Multi finger caliper and TD | – | – |
| 05.2013 | Deep fluid sampling during shut-in | Fluid collected in 2313, 2900, 3500, 4120 m depth | D-Fl |
| 01.2014 | Wellbore cleanout | Samples collected by reverse circulation up to 4346 m | CO |
| 02.2014 | Several production lift tests with simultaneous deep fluid sampling | Deep fluid in 4200 and 4240 m | D-Fl |

TD, total depth; WH-Fl, wellhead fluid; D-Fl, deep fluid; FR, filter residue; CT, coiled tubing; CO, cleanout; B, bailer.

After another production test, a final bailer sample was collected (Table 1). In December 2012, a mechanical multi-finger caliper measurement was performed to measure the inner radius of the well liner (Dennis, 1990). Finally, in December 2013, a work over rig was installed at the production well and after pulling the production pump, the clean out (CO) operation was performed to remove the fill by reverse circulation down to 4346 m. The drilling fluid used was GrSk brine, mixed with near surface groundwater (acidified with HCl to pH 4.5 to remove $HCO_3$) in a mixing ratio of about 1:1 to obtain a fluid density of 1.09 g/$cm^3$.

In May 2013 and in February 2014, deep fluid samples (each 0.6 L) were collected with a Leutert Positive Displacement Sampler (PDS) at in situ P–T conditions at different depths of the production well (Table 1). A detailed description of the fluid sampling procedure is given elsewhere (Regenspurg et al., 2010). While the sampling in May 2013 took place during shut-in, the samples taken in February 2014 campaign were taken immediately after a production lift test thus collecting freshly produced material directly from the reservoir was assumed to be attributed to both the volcanic rock reservoir (sample at 4240 m) and to the sandstone reservoir (sample at 4200 m).

### 2.2. Sample collection, preparation, and analysis

#### 2.2.1. Characterization of solid samples

Four types of solid samples were collected and investigated by various methods (Tables 1 and 2): (I) filter residues (FR) were sampled from filter bags at beginning of circulation tests after each filter change. For this study, seven representative samples out of 107 (collected between July 2011 and December 2012) were analyzed in detail. (II) The first three bailer samples (B) were taken in July 2012 (B115-B117). After a short production test, another bailer was collected (August, 2012, B119). A last bailer sample (B134) was taken after the CT operation. (III) During the CT operation, samples were collected either directly from the fluid return (33 CT samples) or from the storage basin of the returned fluid (three samples). (IV) Samples from the CO operation were obtained either by collecting and filtering the circulation fluid (approximately once per hour with 5 L fluid containing ~5 g solid sample; CO-ff) or by collecting the material directly from the sediment container beneath the vibrating sieve (CO-cf). In both cases, the depth in the well was registered. Sample CO-60 represents a sample collected from a section of the tubing that was clogged at a depth of 4280 m by solid material and transported to the surface by pulling out the entire tubing.

All samples except for a few exceptions (as described later) were collected and stored at oxic conditions. For all sample types the different analytical methods are summarized in Table 2 and described in the following: grain size determinations were carried out either by laser diffraction particle size analyzer (Mastersizer 2000; measurement range: 0.02–2000 μm) for filter residue samples, by wet sieving of samples B 117 and CO 60-, and by microscopy (VHX1000D; zoom objective VH Z20R and VH-Z00R for selected samples. The average mass of filter residues was roughly determined by weighing all (wet) filters. The density and water content of all samples was determined by weighing a defined volume before and after drying at 105 °C. Optical microscopy was used to characterize all sample types (selected samples). For further analyses, dried samples (105 °C) were ground using an agate mortar or a pebble mill to obtain a homogenous powder (63 μm).

Two different methods were applied to determine the elemental composition of the samples: (1) most bailer and CT samples were first extracted with concentrated (65%) $HNO_3$ (1 g/10 mL). The extract was diluted with deionized $H_2O$ (1:5) and the residue was separated by filtration. Both, the extract and the filter residue were kept for analysis. In the extract, the main components were measured (see below). The $HNO_3$-insoluble residue was $H_2O$ washed, dried, ground to a homogenous powder with a mortar and analyzed by the same methods as the original sample. (2) In CO samples, the elemental composition was measured by X-ray fluorescence (XRF) spectroscopy on a Bruker S4 Pioneer instrument, equipped with a 4 kW Rh tube. Major elements were determined at reduced tube energies. Counting times were chosen in a way that the relative $2\sigma$ uncertainties were better than 1% for Si and Al, and better than 5% for elements occurring at the 1–10 wt% concentration level. For the determination of trace elements, tube conditions and counting times were optimized automatically up to 4 kW and 400 s per element, to obtain a detection limit of ~3 ppm ($3\sigma$). Typical errors ($2\sigma$) from the counting statistics were 1–2 ppm at low concentrations (<10 ppm), ~5 ppm at the 100 ppm concentration level, and better than 50 ppm at the 1000 ppm level.

Selected B-, CT-, and FR samples were analyzed for total carbon, nitrogen, and sulfur (CNS), with detection limits of about 0.1 wt% for each species. In five selected CO-cf and CO-ff samples organic and inorganic carbon was measured by a carbon analyzer (Euro EA3000; EuroVector). Total inorganic carbon (TIC) was assumed to correspond completely to calcite which was qualitatively also identified in nearly all samples by a bubbling reaction with 1 M HCl resulting in a visual release of $CO_2$.

**Table 2**
Solid phase analyzes of the different types of samples.

| | Filter residues samples (FR) | Bailer samples (B) | Coiled tubing samples (CT) | Cleanout samples (CO) |
|---|---|---|---|---|
| Grain size distribution | Laser diffraction (mastersizer) | Microscopy, sieving | Microscopy | Microscopy, sieving |
| Mass/density (wet and dry) | Total mass by weighing all filters | Wet/dry density + water content by weighing before and after drying (105 °C) | | |
| Elemental composition | XRF, CNS Analyzer | Extraction + ICP or XRF (one sample), CNS analyzer | Extraction + ICP | XRF, TC/TOC or elemental analyzer |
| Mineral composition | | XRD, SEM + EDX | | |
| Magnetic properties | Magnetic susceptibility | Mössbauer spectroscopy | Not measured | Mössbauer spectroscopy |

The mineral composition was determined in solid samples by powder X-ray diffraction (XRD) which was carried out in transmission with a Cu Kα1 radiation source. The diffractometer was equipped with a primary monochromator and a 7°-wide position 9 sensitive detector. Diffractograms were semi-quantitatively evaluated by the software EVA as well as by Rietveld refinement. Scanning electron microscopy (SEM) was applied with a beam current acceleration of 20 kV, and a maximum aperture of 120 μm. On selected image spots, the material composition was semi-quantitatively characterized by energy dispersive X-ray (EDX), using the same accelerating voltage.

### 2.2.2. Sampling and analysis of magnetic mineral phases

The magnetic mineral phases were removed from the bulk samples by a bar magnet, washed with deionized water, and analyzed by XRD, SEM, and XRF to determine the mineral and chemical composition. Additionally, magnetic susceptibility was analyzed on dried samples of five FR – and of one B sample (119). Temperature dependent magnetic susceptibility was measured with a KLY-3 Kappabridge (AGICO) with a peak magnetic field intensity of 300 A/m and a frequency of 875 Hz with an attached CS-3 furnace. Experiments were conducted in air between room temperature and 700 °C with a heating rate of 5 °C/min.

The magnetically extractable components of CO samples (43, 109, 60-1 and 60-5) and B sample 117 were analyzed by $^{57}$Fe Mössbauer spectroscopy. After collecting about 20 mL of the wet material in the field, samples were sealed immediately in glass vials and prepared in an anoxic glovebox (100% $N_2$). After grinding and separating the magnetic components they were transferred to Eppendorf tubes (2 mL) and passed through a filter (0.45 μm, mixed cellulose esters, Millipore) to remove the aqueous phase. The filter and sample were then sealed between two layers of oxygen-impermeable adhesive polyimide film (Kapton) and stored in a Schott bottle for transfer to the Mössbauer instrument. Each sample was inserted into a closed-cycle exchange gas cryostat (Janis cryogenics) and all spectra were collected at 77 K using a constant acceleration drive system (WissEL) in transmission mode with a $^{57}$Co/Rh source and calibrated against a 7 μm thick α-$^{57}$Fe foil measured at room temperature. All spectra were analyzed using Recoil (University of Ottawa) by applying a Voigt Based Fitting (VBF) routine (Rancourt and Ping, 1991). The half width at half maximum (HWHM) was fixed to a value of 0.122 mm/s for all samples, which was determined from the inner line broadening of the calibration foil at room temperature.

### 2.2.3. Sampling and analysis of aqueous solutions and $HNO_3$ extracts

Deep fluid samples have been collected from various depths of the production well (in May 2013 at 1700, 2900, 3500, and 4100 m during shut-in and in January 2014 at 4200 and 4240 m immediately after a lift test). After degassing, all samples were immediately filtered (0.2 μm). One subsample of the liquid was acidified to pH 1–2, and a second subsample was directly analyzed for chemo-physical parameters (see below) and for anions by ion chromatography within few days after sampling.

Methods used for sample preparation and analysis of fluid chemical and physical parameters are described in detail by Feldbusch et al. (2013). Total elemental composition (K, Na, Li, Cu, Si, Al, Ca, Mg, Ba, Fe, Mn, Sr, Cr, Cd, Pb, Zn, As, Ni, Hg, Ag, B, Ge, Ti, Co, and W) was analyzed by inductive coupled plasma mass spectrometry (ICP-MS) in aqueous acidified samples as well as in the $HNO_3$-extract of bailer sample 115. The measurement uncertainty for all elements measured by the used methods with ICP varies between 8 and 12%. In all other extracts, only the main components (>0.4 wt%: Ca, Fe, Pb, As, Cu, Hg) were analyzed. In non-acidified samples, anion concentrations were measured by ion

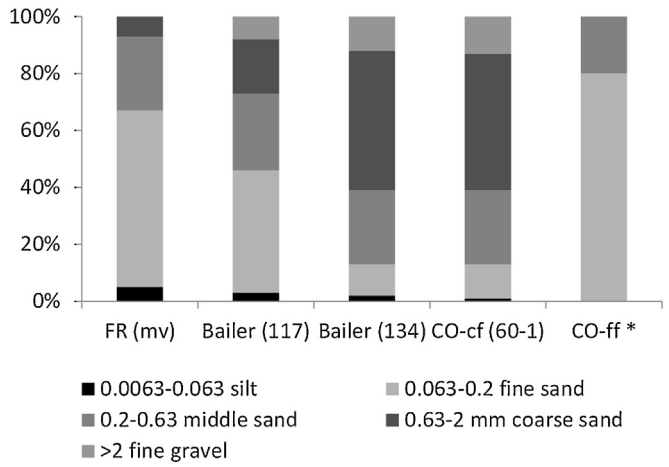


**Fig. 3.** Grain size distribution for filter residue samples (mean value of about 50 samples measured by Mastersizer), bailer samples collected before- (B 117), and after (B134) the CT operation (by wet sieving), and cleanout samples CO-cf (coarse fraction, measured by wet sieving), and CO-ff sample (fine fraction, estimated from microscopy).

chromatography with analytical uncertainty of <5%. The pH value, which was also measured in pore water from bailer samples, was determined by Ag/AgCl electrodes. Measured pH values require a correction due to the salinity depended shift in hydronium activity (Altmaier et al., 2003). The shift has been determined for the applied electrode to be about 1.1 pH units (Feldbusch et al., 2013). All pH values presented here are shift corrected.

### 2.3. Geochemical equilibrium calculations

For estimations of mineral saturations, concentrations, and metal speciation, equilibrium calculations were performed with the geochemical program PhreeqC version 3.1.2 (Parkhurst and Appelo, 2011). As input file, a 1.5 M $CaCl_2$ plus 2 M NaCl solution with 1 mM of either $Pb^{2+}$, $Cu^{2+}$, or $Ba^{2+}$ and $SO4^{2-}$, and variation of pH (4–10) and temperature (20–150 °C) was selected. Due to high salinities of the fluid, calculations require the application of Pitzer activity coefficients (Pitzer and Mayorga, 1973), which are however unavailable for many species. Only few databases such as the Quintessa Ltd. (pers. communication) are known to have compiled and available Pitzer parameters that have been translated to PhreeqC. Quintessa in turn, translates the EQ3/6 database (Sandia National Laboratories, 2007) but it is not peer-reviewed and for evaluation purposes only. The recently developed GeoDat database was validated with experimental data over a wide range of ionic strength and temperature especially for some systems relevant for geothermal application such as barite saturation (Moog and Cannepin, 2014). Since many minerals are not considered by these databases however, calculations for laurionite were made with the LLNL database (Johnson et al., 1992; Wolery, 1992) which implies at least paralaurionite (the more amorphous form of laurionite). These results however, can be used for rough estimation only since more correct calculations require application of Pitzer activity coefficients.

Barite saturation was calculated for comparison with all three databases (Quintessa, GeoDat, and LLNL). For metal speciation of aqueous complexes the Geodat database was used.

## 3. Results

### 3.1. Characterization of precipitates

#### 3.1.1. Visual description and particle size distribution

Filter residue samples are fine grained (0.1–1 mm Ø; fine sand fraction) and of brownish to grayish color. No individual minerals can be determined visually or by optical microscope in FR samples. Bailer samples are dark grayish-brown and of larger grain size (mainly 1–2 mm of average Ø; middle to coarse sand fraction) with occasionally 10 mm Ø particles; Fig. 3). The largest particles of mainly coarse sand fraction were found in bailer sample 134 (Fig. 3), collected after the CT operation (thus being disturbed of the original sedimentation stratigraphy). Grain size distribution of CT and CO samples, as observed by microscopy, differed strongly depending on if they were collected directly from the drilling fluid in which case the material was very fine grained and homogenous (<0.05 mm) or if they were collected from the storage containers for solid disposal. The latter material was mainly composed of larger particles similar to bailer samples. Therefore, the CO fine fraction (CO-ff) is differentiated from the CO coarse fraction (CO-cf). In the rather coarse grained CT, CO as well as in B samples small nuggets (1–10 mm) of native copper as well as laminated gray and white particles (1–2 mm) are visible (Fig. 4). Some of the CO-cf samples were almost completely composed of tabular shaped particles of 2–3 mm length (Fig. 4). Most samples also contained a small fraction (1–2 wt%) of dark-brown-black, particles that can be separated

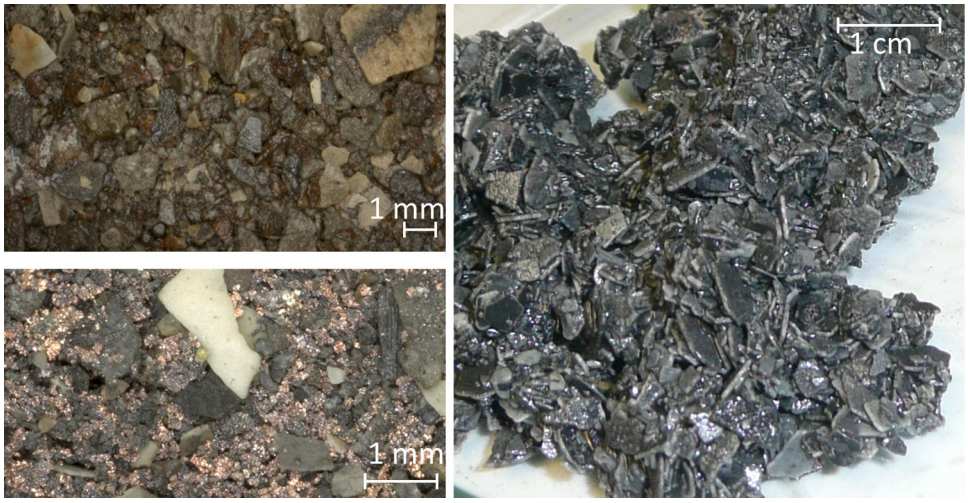


**Fig. 4.** Left: Microscope images of a CT sample (top) and a B sample (117; bottom) with shiny copper particles. Right: Photograph of CO (60-1) sample with tabular copper particles coated with a gray layer (presumably cuprite).

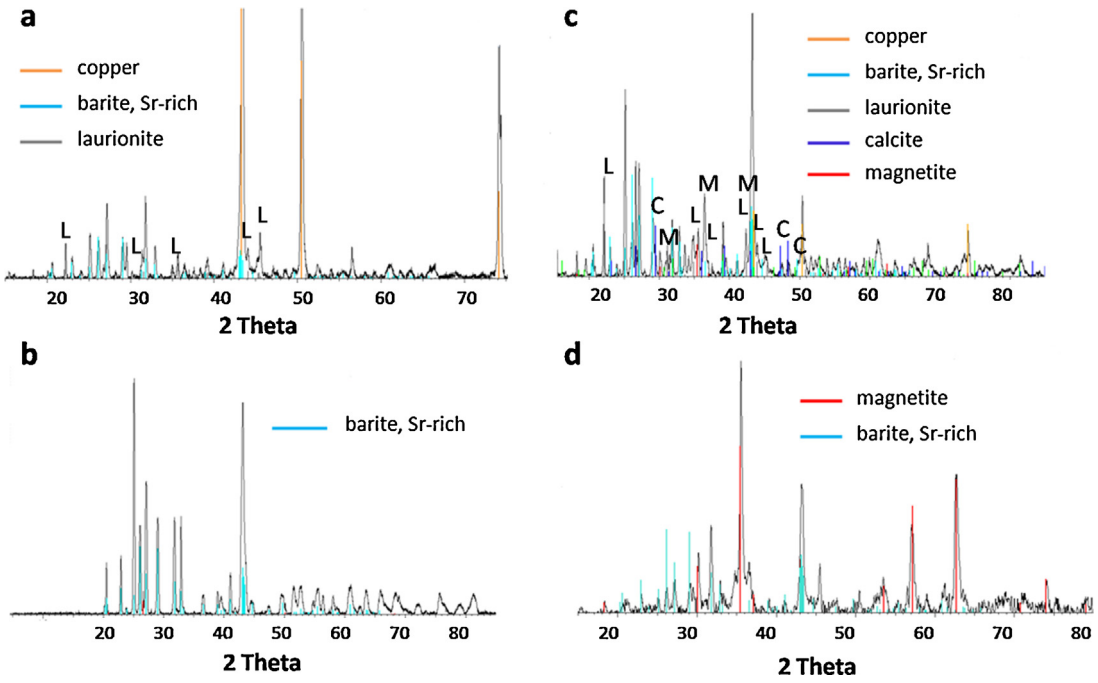


**Fig. 5.** Powder X-ray diffractograms of a bulk bailer sample (115) before (top left) and after (bottom left) extraction with 65% $HNO_3$ as well as a FR sample (top right) and a magnetically separated phase (bottom right). The *y*-axis gives the intensity, letters indicate reflex lines of minerals less obvious to identify (M: magnetite; L: laurionite; C: calcite).

by a magnet. All samples collected directly from the cleanout fluid (CO-ff samples) consisted predominantly out of this black magnetic material with an associated carbonate phase (presumably calcite) as indicated by strong reaction with 1 M HCl.

### 3.1.2. *Mineral and chemical composition of the fill*

All sample types are predominantly composed out of the following phases as identified by XRD and confirmed by determination of the elemental composition: strontium (Sr)-rich barite ($(Sr,Ba)SO_4$), native copper ($Cu^0$), laurionite (PbOHCl), magnetite ($Fe_3O_4$), calcite ($CaCO_3$), and a large fraction of amorphous material containing mainly Si, Ca, Al, Pb, and Fe. Some representative examples of X-ray diffractograms are shown in Fig. 5a–d. Occasionally, small amounts of other minerals such as cuprite ($Cu_2O$), copper oxide (CuO), and rarely quartz ($SiO_2$) were identified in B and CO samples. XRD evidenced that the $HNO_3$ extraction as performed in B and CT samples readily dissolved (35–85 wt%) all minerals apart from the (Sr-rich) barite (Fig. 5a and b). Apart from traces of quartz and possibly calcite, no reservoir-rock minerals such as feldspars, hematite, or clay minerals could be identified.

Individual crystals of the four sample types were analyzed by SEM in combination with EDX to determine crystal morphology and their elements ratio concentration (Fig. 6). EDX confirmed the barite to be Sr-rich with a Ba:Sr ratio of about 4:1. Barite crystals of all sample types typically showed well-defined tabular–laminar shapes of different sizes, whereas laurionite crystals are of regular shape, sometimes in radial aggregations (Fig. 6). Apart from barite, particles in the filter residue samples showed rather indefinite morphologies with heterogeneous elemental composition (e.g. Ca–Si–Fe compounds). Copper typically occurred as fine polycrystalline grains (Fig. 4), in thin laminated, or in tabular–dodecahedral shapes (Figs. 4 and 6) often covered with a metallic-grayish layer (Fig. 4, right) which was identified as cuprite by XRD, EDX and optical appearance.

Analysis of total elemental composition by XRF and CNS revealed that the following five elements predominated in all samples: Cu, Pb, Ba, Fe, and S (Table 3). This confirms results from XRD that showed native copper, laurionite and barite to be the most prominent minerals. Total sulphur content was found to vary between 2 and 10% and assumed to correspond completely to the sulfate of barite due to stoichiometric correlation with total Ba (Regenspurg et al., 2014). XRF allows, in combination with XRD, a rough quantification of the mineral composition by assuming that all Cu is present as native copper, all S and Ba as barite, and all Fe as magnetite (Fig. 7) although $^{57}$Fe Mössbauer results indicate the presence of some other Fe phases in the samples (Section 3.1.3). Since Pb occurs as laurionite, native lead, and as an amorphous phase, this simplified estimation cannot be made for Pb minerals.

**Table 3**
Mean values of main element composition (wt%) of all samples of the different sample types determined either after dissolution of various samples in $HNO_3$ by ICP (B, FR, CT) or by XRF (CO) and calculated to total weight percentage of the sample. Total S in FR, CT, and B samples was determined in bulk samples by CNS.

| Sample type | Si | Ba | Cl | Cu | Fe | Pb | Ca | As | Hg | S |
|---|---|---|---|---|---|---|---|---|---|---|
| B[a] | 1.3[b] | 8.4[b] | 7.7[b] | 49.1 ± 1.6 | 1.26 ± 0.6 | 7.6 ± 5.5 | 2.23 ± 1.1 | 0.7 ± 0.1 | 0.4 ± 0.02 | 3.09 ± 0.1 |
| FR | 2.85 ± 2.35 | 2.08 ± 1.6 | nm | 4.76 ± 2.4 | 3.57 ± 2.2 | 2.6 ± 4.5 | 7.28 ± 4.75 | 0.16 ± 0.2 | 0.14 ± 0.1 | 5.4 ± 3.5[c] |
| CT | 0.12 ± 0.14 | 4.96 ± 0.5 | nm | 25.6 ± 17 | 5.04 ± 3.1 | 6.1 ± 11 | 2.5 ± 2.0 | 2.04 ± 1.3 | nm | 1.4 ± 0.4 |
| CO-ff | 2.34 ± 0.32 | 1.8 ± 0.28 | 4.1 ± 0.9 | 5.3 ± 0.36 | 11.4 ± 0.7 | 3.8 ± 0.7 | 5.7 ± 1.1 | nm | 0.45 ± 0.03 | 0.48 ± 0.25 |
| CO-cf | 2.2 ± 1.1 | 16.4 ± 7.8 | 5.8 ± 3.5 | 25.4 ± 15.7 | 0.73 ± 0.4 | 8.1 ± 6.5 | 2.68 ± 1.3 | 0.27 ± 0.17 | 0.65 ± 0.3 | 4.5 ± 2.8 |

[a] Without B134.
[b] Determination of one sample by XRF.
[c] Average of 40 samples.

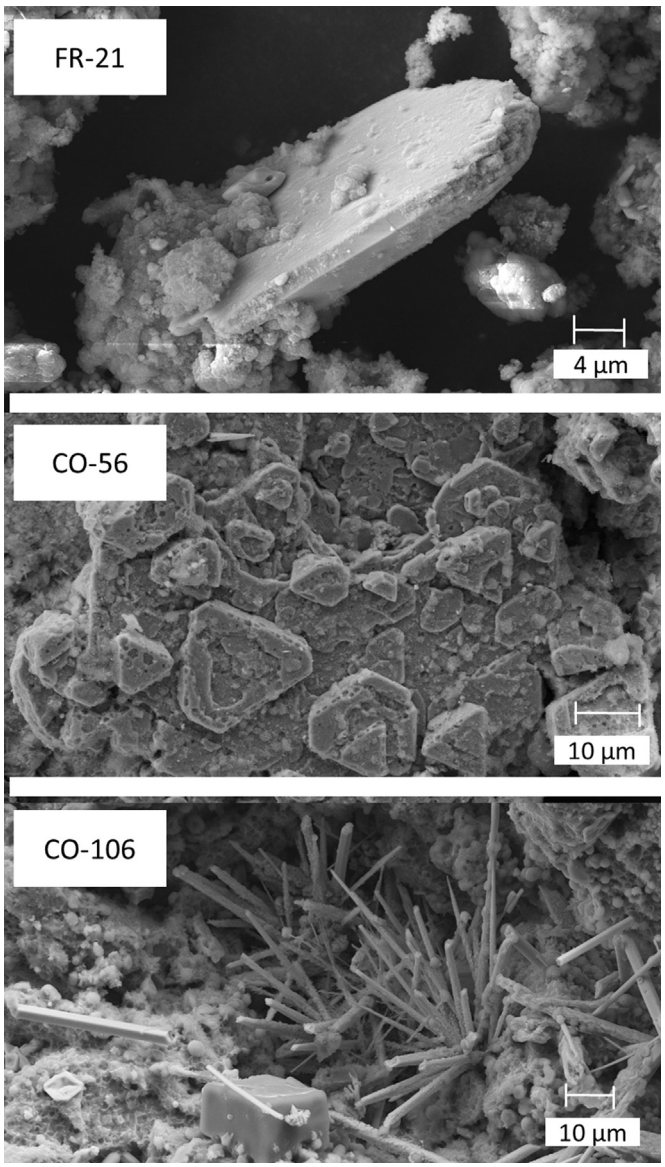


**Fig. 6.** Scanning electron micrographs. Morphologies were identified by EDX as tabular Sr-rich barite (top), tabular native copper with copper oxide layer (middle), and needle shaped, radial grown laurionite (bottom).

The relative amounts of the respective minerals differ strongly depending on the sample types or sampling procedure, respectively. Bailer samples collected before the CT operation can be considered as most "autochthonous" sample types with highest amounts of native copper (50%). The bailer sample collected after the CT operation (B134; Table 1), however, consisted predominantly of barite (65 wt%) indicating the CT strongly disturbs the mineral stratification and separates them according to size, shape, and density of the grains. Similarly, the Cu content is decreased in CT, CO and especially FR samples (Fig. 7) indicating that high density copper particles are hardly removable from the well depth by flushing and pumping activities (density of copper at room temperature: 8.92 g/cm$^3$). Consequently, all analyzed data of samples collected by these methods show high error bars (Fig. 7). CO-ff samples are relatively homogenously composed of predominantly magnetite and calcite (Fig. 7).

All samples additionally contain relatively high amounts of arsenic (As) and mercury (Hg) which both correlate well with the samples Cu content (up to 2 wt% As and 0.7 wt% Hg, resp.; Table 3).

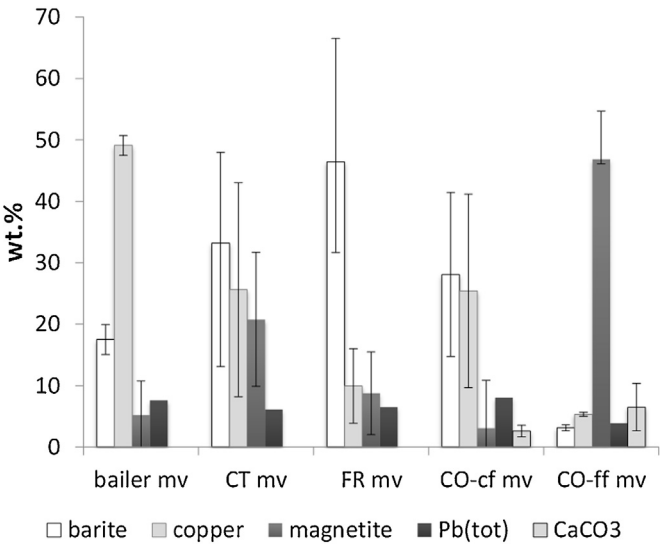


**Fig. 7.** Mineral composition (mean values; mv) as calculated from elemental analysis and XRD results with standard deviation for all bailer (B) samples except B134, CT (coiled tubing), FR (filter residues), CO-cf (clean out coarse fraction), and CO-ff (clean out fine fraction) samples.

Depth profiles of main elemental distributions (Ba, Pb, and Cu), as determined by XRF analysis, was performed for all CO-cf samples (Fig. 8). Apart from Pb which decreases with depth, there is apparently no obvious elemental profiling and metal content is highly

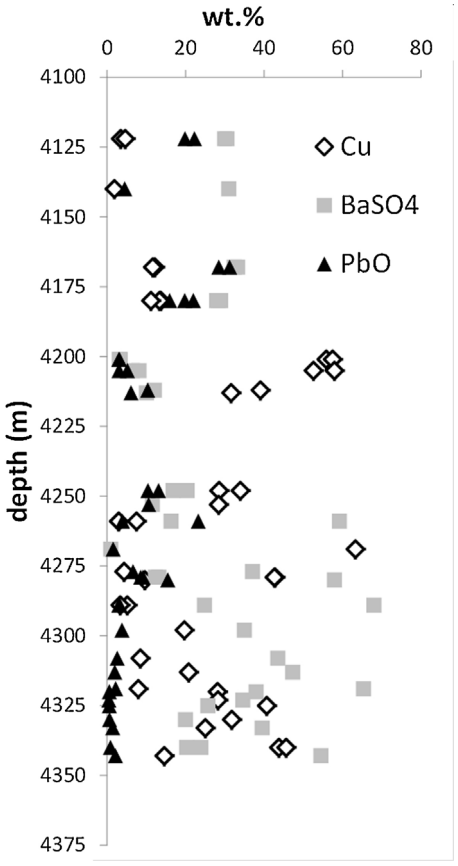


**Fig. 8.** Depth profiles of main mineral composition as calculated from elemental analysis (native copper, $BaSO_4$, and total Pb as PbO) in the coarse fraction of well bore cleanout samples (CO-cf).

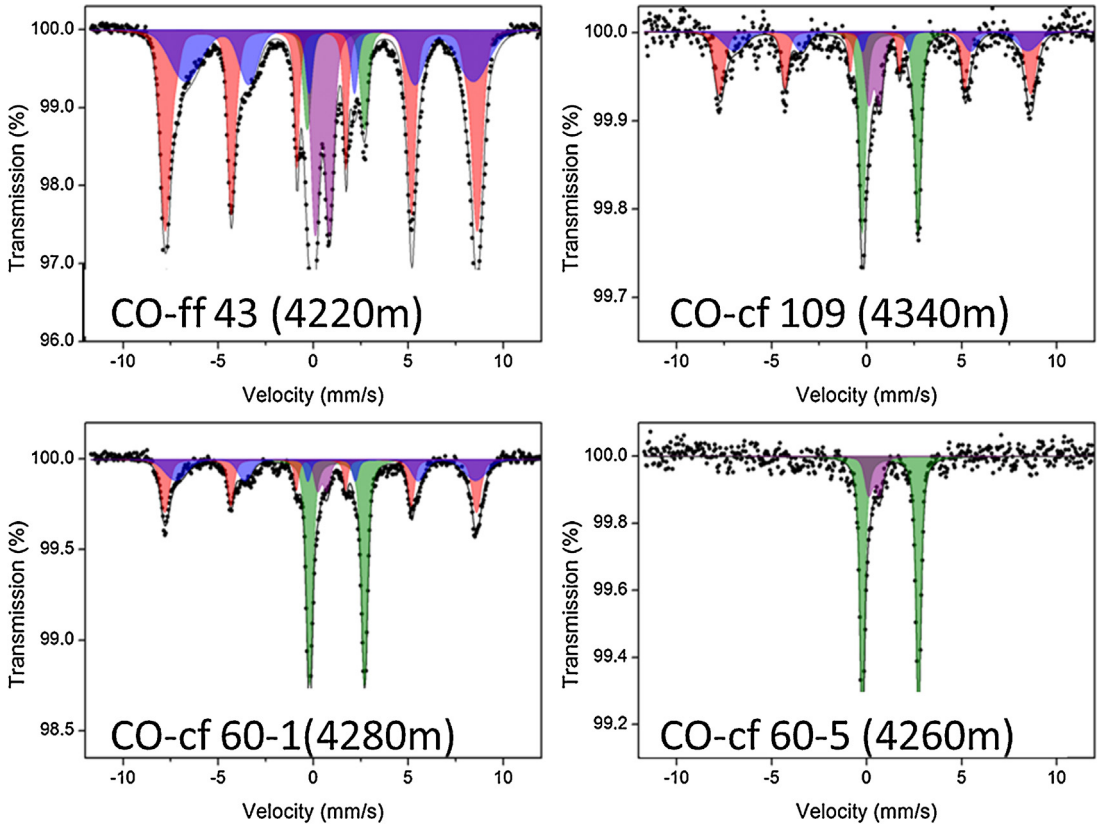


**Fig. 9.** Mössbauer spectra recorded at 77 K of samples CO-cf 43, CO-cf 109, CO-cf 60-1, and CO-cf 60-5. Magnetite sextets consist of tetrahedral (red) and octahedral sites (blue). Doublet features correspond to $Fe^{2+}$ mineral phases (green) and $Fe^{3+}$ mineral phases (purple). (For interpretation of the references to color in this figure legend, the reader is referred to the web version of this article.)

variable in all depths of the borehole. The appendix shows all measured XRF data from CO samples.

Total carbon (up to 3% in B samples-, up to 12 wt% in FR and CO-cf samples, and up to 5% in CO-ff samples) can be linked to both, inorganic carbonates such as calcite and to organic carbon. Total organic carbon as determined in CO-cf samples was found to represent 66–83% of total carbon.

### 3.1.3. *Characterization of the iron mineral phase*

Although iron is present in all samples, its content is highly variable with lowest concentration in the bailer and CO-cf (coarse) fraction and highest content (up to 11.4 wt% Fe) in the CO-ff (fine) fraction (Table 3), which accounts for up to 50% magnetite ($Fe_3O_4$; Fig. 7). Most of Fe occurred as fine black, magnetic powder. The magnetically separated fraction showed relatively broad peaks in the XRD pattern corresponding to poorly crystalline magnetite (Fig. 5d). The presence of magnetite was confirmed by measuring the T-dependent magnetic susceptibility which determines the material specific Curie temperature ($T_c$; temperature above which a magnetic material will become disordered and no magnetic moment can be detected) in one B and 5 FR samples. All six samples measured display $576\,^{\circ}C < T_c < 591\,^{\circ}C$ consistent with the presence of magnetite. However, since all samples were prepared and analyzed in air, the formation of magnetite by oxidation of another Fe(II)-containing mineral by atmospheric oxygen must be considered. To verify this, Mössbauer spectroscopy, was used to determine Fe speciation and redox state in one B (B116), one CO-ff- and three CO-cf samples that have been stored and analyzed at anoxic conditions. All spectra show some similar but distinct characteristics when measured at 77 K with magnetic mineral phases (seen as sextets) and paramagnetic mineral phases (seen as doublets); Fig. 9. By considering the center shift (CS) and quadrupole splitting ($\Delta E_Q$) of the doublets, the oxidation state of the iron can be determined. Specifically, a CS value of <0.8 mm/s combined with a $\Delta E_Q < 1$ mm/s is characteristic for Fe(III) minerals whereas, high spin Fe(II) shows CS values >1.05 mm/s and $\Delta E_Q > 1.3$ mm/s (Table 4). Consequently, all samples contain some Fe(II) and Fe(III) paramagnetic mineral phases in varying relative amounts.

The sextet feature which is observable in samples CO43, CO109, and CO60-1 (Fig. 9) requires the use of two individual sites. This is a characteristic requirement of the mineral magnetite ($Fe_3O_4$) which consists of Fe in both tetrahedral and octahedral sublattices. These sublattices are given the notation (A) and (B), corresponding to the tetrahedral and octahedral sites, respectively. Closer examination of the parameters (Table 4) indicates that the sextets are closely matched to those expected for magnetite (Murad, 2010). The absence of any magnetite in sample 60-5 does not necessarily mean that it is not present; however, it is likely to be present in lower concentrations than the detection limit of the instrument (~5%).

The Fe(II) component which is clearly visible in all of the samples generally exhibits very similar parameters in all spectra (Fig. 9) suggesting the same mineral species with similar characteristics to the mineral olivine $(Mg^{2+},Fe^{2+})_2SiO_4$ (Bancroft et al., 1967). XRF measurements confirmed the presence of both Mg and Si in all samples but since olivine was neither identified by XRD nor could it be expected in this kind of host rock, rather an amorphous Fe–$SiO_4$ phase must be assumed.

The paramagnetic Fe(III) phase which is present in all samples seems to correspond to a poorly crystalline mineral. This phase is most highly abundant in sample 43 with a center shift of 0.49 mm/s,

**Table 4**
Fitting parameters for Mössbauer measurements obtained for samples measured at 77 K.

| Sample | Site | Temp. (K) | CS (mm/s) | $\Delta E_Q$ (mm/s) | $\varepsilon$ (mm/s) | <\|H\|> (T) | Pop. | ± |
|---|---|---|---|---|---|---|---|---|
| CO-ff 43 | Fe(II) | 77 | 1.2 | 3.01 | | | 8.4 | 0.3 |
| | Fe(III) | | 0.49 | 0.76 | | | 17.6 | 0.3 |
| | Mag. (A) | | 0.43 | | −0.01 | 50.5 | 45.8 | 0.6 |
| | Mag. [B] | | 0.92 | | −0.06 | 46.9 | 28.3 | 0.7 |
| CO-cf 109 | Fe(II) | 77 | 1.24 | 2.92 | | | 35.1 | 2.3 |
| | Fe(III) | | 0.39 | 0.57 | | | 13.9 | 1.5 |
| | Mag. (A) | | 0.44 | | 0 | 50.8 | 32 | 3.1 |
| | Mag. [B] | | 0.89 | | −0.13 | 47.9 | 19 | 3.6 |
| CO-cf 60–1 | Fe(II) | 77 | 1.26 | 2.89 | | | 43.7 | 1.3 |
| | Fe(III) | | 0.48 | 0.49 | | | 6 | 0.6 |
| | Mag. (A) | | 0.41 | | −0.01 | 50.9 | 26.8 | 1.3 |
| | Mag. [B] | | 0.82 | | −0.15 | 48.9 | 23.4 | 1.7 |
| CO-cf 60–5 | Fe(II) | 77 | 1.25 | 2.96 | | | 83.7 | 2.3 |
| | Fe(III) | | 0.39 | 0.57 | | | 16.3 | 2.3 |
| B116 | | | | | | | | |
| | Db1 | 140 | 1.24 | 2.74 | | | 100 | |
| | Db1 | 140 | 1.23 | 2.76 | | | 87.6 | 1.4 |
| | Db2 | | 0.68 | 0.37 | | | 5.1 | 0.8 |
| | Sextet | | 0.699 | 0.778 | | 50.2 | 7.4 | 1.3 |
| | Db1 | 77 | 1.25 | 2.82 | | | 91.3 | 1 |
| | Db2 | | 0.678 | 0.377 | | | 2.9 | 0.5 |
| | Sextet | | 0.672 | | −0.396 | 50 | 5.8 | 0.9 |

CS – center shift with respect to α-$^{57}$Fe foil standard, $\Delta E_Q$ – quadrupole splitting; $\varepsilon$ – quadrupole shift (note that $\Delta E_Q = 2\varepsilon$), <|H|> – mean hyperfine field; Pop. – relative population. Sample B116 was measured at three different temperatures.

and quadrupole splitting of 0.76 mm/s (Table 4). These values show close similarity to ferrihydrite measured at 77 K (Sharma et al., 2010; Murad and Cashion, 1980). The parameters for the Fe(III) phase in the other samples show some slight differences to each other, however it is likely that they all also correspond to ferrihydrite.

### 3.2. Characterization of the aqueous phase

In the production well, deep fluid samples were collected at 1200, 1800, 3500, and 4120 m in May 2013 during shut-in phase and at 4240 and 4200 m immediately after a lift test in 2014. Table 5 gives an overview of major and minor components in the samples and compares them with a very pristine fluid that has been collected in 2001 in the injection well immediately after drilling as well as to samples collected at the well head above ground in 2011 (Feldbusch et al., 2013; Regenspurg et al., 2010). The pH values range between 6.2 and 7.7 and concentrations of major elements are relatively similar. The two samples collected right after the lift test (in 2014), represent dominant contributions of two different geological formations that have been stimulated: the volcanic rock (4240 m) and the sandstone (4200 m). These two samples show differences in overall salinity as well as of major and minor ions. Certain minor components, especially Fe, Pb, and sulfate are relatively variable in their concentration indicating they are more reactive elements. Copper concentration is low (<0.5 mg/L) with only the sample collected in 2001 showing a higher concentration of 7 mg/L and the two "fresh" samples collected after the lift in 2014 with 0.5 and 18 mg/L (Table 5). Additionally, two outlier extreme values were measured in samples collected during a sampling campaign in 2011 with 2 and 98 mg/L, respectively (Table 5).

### 3.3. Quantification of precipitates and material loss of the casing

A rough estimation of the total mass of the solid phase of the four sample types (FR, B, CT, and CO) removed from the borehole was derived from simple gravimetric and volumetric measurements. Filter bags removed altogether about 1500 kg (dry) material (1176 filters have been changed with an average load of 1275 g per filter) over the production time. Bailer samples collected about 3 L of material (6.6 kg). During the CT operation about 70 L of material with mean density of 2.0 g/cm$^3$ (140 kg) was flushed out and during the well cleanout about 224 L coarse grained material (density 2.1 g/cm$^3$) and 172 L fine-grained material (1.1 g/cm$^3$) were flushed out. Thus, altogether about 2300 kg of solid phase have been removed from the well.

Not all of the produced solid material, however, derives from the reservoir fluid. Measurements of the inner radii of the well bore liner by multi finger caliper showed an increase in the 5″ liner as compared to the nominal radius, indicating a material loss. At the bottom of the logged section, the average inner radius is about 1 to 1.3 mm larger and toward the top, the radial difference decreases to about 0.7 mm, corresponding to an apparent metal loss of about 12% at the bottom and 7% at the top, respectively. The 7″ liner, measured in comparison between 2333 and 2768 m even showed only a material loss of about 2.6%.

### 3.4. Geochemical equilibrium calculations

Speciation calculations by PhreeqC indicate that aqueous Pb and Fe species occur at given salinities, 150 °C, and neutral conditions to 85–95% as negatively or uncharged chloride aquo complexes (predominantly as $PbCl_3^-$, $PbCl_2$, $FeCl_2$, $FeCl_3^-$). Upon cooling, the amount of positively charged complexes increases slightly (up to 10% for $FeCl^+$ and 25% for $PbCl^+$). Copper might occur as Cu(I) or Cu(II) chloride complexes (positively or uncharged) or free $Cu^{2+}$ in approximately equal proportions. Barium, in contrast occurs as about 50% positively charged chloride $BaCl^+$ and 50% $Ba^{2+}$. Fig. 10a shows the mass of barite that could precipitate at various temperatures starting from an equilibrium Ba and sulfate concentration (1.5 mM) as calculated by the program for 150 °C. Depending on

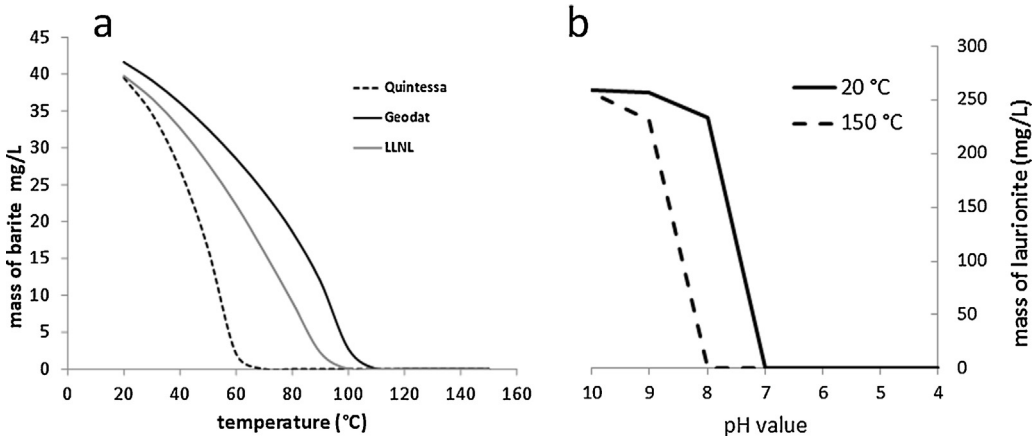


**Fig. 10.** Equilibrium calculations performed with PhreeqC 3.1.2 (a): calculated amount of barite that would precipitate out of 1 L fluid in dependence of temperature starting from equilibrium temperature (150 °C) concentration at pH 7 using three different databases. (b) Laurionite precipitation is shown as function of pH and temperature; calculated with the llnl database as paralaurionite.

the type of database used, precipitation would start between 70 and 130 °C. Calculation of laurionite precipitation was performed with the LLNL database revealing that laurionite precipitation increases strongly with pH and decreasing temperature (Fig. 10b). At pH-values above 7.2, laurionite precipitation is very likely to happen whereas at pH 7 only below 20 °C oversaturation occurs (Fig. 10b).

## 4. Discussion

Roughly two tons of solid material precipitated during production of about 20,000 $m^3$ fluids in the Groß Schönebeck geothermal production well. The main components of this scaling material that were removed by different operations (filtering, coiled tubing, bailer and clean out operation) include native copper, Sr-rich barite, laurionite (and other Pb phases), and magnetite. Potentially, some of these minerals formed not only the fill of the production well but may have also precipitated within the perforations of the liner or in the pores of the reservoir rock. Thus they could contribute to the decrease in productivity that has been observed over time along with material loss of the steel liner that eventually resulted in the shut-down of the plant.

Shifts of the chemical equilibrium in geothermal fluids have to be expected due to drilling, borehole completion, stimulation, and fluid production that might result in scaling and corrosion. To prevent further scaling in this and similar geothermal settings it is crucial to understand the chemical reactions governing the observed precipitation. In the following sections relevant reactions, mineral formation pathways, and the origin of scale forming metals are discussed.

When looking at the results, it must be taken into account that although all samples derive from the same borehole, they were sorted according to their grain size, shape, and density. While filter residues are most likely to be the smallest and lightest particles, bailer samples collected before the CT operation should be less disturbed in comparison to the other sample types. During CT and wellbore cleanout, a strong segregation can be expected. Additionally, chemical reactions with the drilling fluid or atmospheric oxygen during sample collection and storage must be considered.

### 4.1. Formation of barite

All samples collected at the GrSK site contain substantial amounts of barite (15–85 wt%). The occurrence of this poorly soluble mineral is frequently observed in scales of oil and gas wells (Collins, 2005; Bin Merdhah and Yassin, 2007; Shen et al., 2009) with many studies investigating its formation and solubility in geothermal fluids (Blount, 1977; Monnin and Galinier, 1988, 1998). For example, at the geothermal field in the Californian Salton Sea, barite was found to precipitate in the injection well as consequence of cooling down the brine (McLin et al., 2006).

The GrSk reservoir rocks contain a small amount of barite (400–12000 ppm Ba; Regenspurg et al., 2014; Trautwein, 2005), which is most likely in equilibrium with dissolved Ba and sulfate concentrations at reservoir conditions. The measured concentrations are about 0.2–0.4 mM Ba and 0.02–2 mM sulfate (Table 5) which is below or close to barite saturation concentration at room temperature. Therefore, it can be assumed that barite precipitation takes place immediately upon cooling of the sample (e.g. during uplift of the PDS sampler in the well) and that the reservoir concentration of Ba and sulfate is in fact higher. Their calculated equilibrium concentration at a reservoir temperature of 150 °C amounts to 1.5 mM (or 144 mg/L sulfate and 205 m/Lg Ba). PhreeqC was used to calculate the amount of precipitated barite that could have formed upon cooling. This concentration varies significantly depending on the database used (Geodat, compared to Quintessa and Llnl; Fig. 10a). The results obtained with Geodat are considered as most realistic because these data have been experimentally validated especially for the barite system (Moog and Cannepin, 2014). Accordingly, a temperature decrease from 150 °C to 80 °C could precipitate up to 400 kg of barite after producing 20,000 $m^3$ brine (roughly the amount so far produced at the GrSk site). However, calculations do not consider solid solutions of Sr and Ba that were observed at the GrSk site.

Throughout the time of the circulation tests, it was not only observed that with increased wellhead temperature (corresponding to continuous fluid production), the overall amount of precipitation decreased (indicated by fewer filter changes) but also that barite crystal sizes in filter residue samples increased (data not shown). In general, bailer samples contained less barite as compared to filter residues and CT samples (Fig. 7) with mainly larger-sized crystals. This indicates that the small-sized barite particles are predominantly removed by fluid production and filtration whereas the larger particles are deposited at the bottom of the well, where they remain due to the low solubility of barite. Bailer sample B134, collected after the CT operation consisted predominantly of large crystals (few mm) of barite confirming that the CT operation strongly disturbed the material profile at the bottom of the well and the grains settled down according to size and mass. Despite its high density (4.48 g/$cm^3$), barite is still less heavy in comparison to the other two main minerals identified (laurionite: 6.24 g/$cm^3$ and

**Table 5**
Properties of fluid samples collected at various depths of the production well (May 2013 and January 2014) compared to a deep fluid sample collected at the injection well (IW) in 2001 at 4200 m (reference sample), and to samples collected during a production test at the production well (PW) head (Aug-Nov 2011).

| Well; sampling date; depth (m) | pH | Na (g/L) | K (g/L) | Ca (g/L) | Mg (mg/L) | Fe (mg/L) | Mn (mg/L) | Al (mg/L) | Li (mg/L) | B (mg/L) | Si (mg/L) |
|---|---|---|---|---|---|---|---|---|---|---|---|
| PW;2013; 2313 | 7.4 | 37.7 | 3.60 | 54.8 | 395 | 174 | 215 | 0.01 | 219 | 131 | 4.59 |
| PW;2013; 2900 | 7.6 | 38.0 | 2.62 | 52.9 | 344 | 95.3 | 167 | 0.02 | 203 | 130 | 3.41 |
| PW;2013; 3500 | 7.6 | 39.6 | 3.12 | 53.8 | 382 | 63.5 | 148 | 0.02 | 215 | 132 | 2.89 |
| PW;2013; 4120 | 7.7 | 39.2 | 2.74 | 54.0 | 397 | 47.8 | 201 | 0.08 | 212 | 142 | 3.02 |
| PW;2014 4200 | 6.3 | 40.9 | 2.96 | 51.2 | 364 | 51.5 | 222 | 0.068 | 237 | 147 | 41.2 |
| PW; 2014 4240 | 7.1 | 33.6 | 2.56 | 45.4 | 233 | 47.1 | 131 | 0.036 | 212 | 116 | 43.8 |
| IW;2001, 4200[a] | 6.8 | 38.4 | 2.9 | 54 | 430 | 114 | 270 | nm | 204 | nm | 37 |
| PW;2011; well head[b] | 6.2–7.2 | 34.3–40.6 | 2.9–3.5 | 42.5–48.6 | 298–354 | 62–116 | 171–201 | 0.03–0.1 | 198–216 | 109–131 | 37–41 |

| Well; sampling date; depth (m) | Cu (mg/L) | Zn (mg/L) | As (mg/L) | Sr (mg/L) | Cd (mg/L) | Ba (mg/L) | Hg (mg/L) | Pb (mg/L) | Cl (g/L) | $SO_4$ (mg/L) |
|---|---|---|---|---|---|---|---|---|---|---|
| PW;2013; 2313 | 0.05 | 105 | 0.010 | 1540 | 1.18 | 58.8 | 3.29 | 2.29 | 160 | 190 |
| PW;2013; 2900 | 0.25 | 87.6 | 0.05 | 1520 | 0.75 | 44.7 | 8 | 2.52 | 142 | 144 |
| PW;2013; 3500 | 0.1 | 102 | 0.02 | 1570 | 0.845 | 47 | 14.3 | 1.4 | 144 | 175 |
| PW;2013; 4120 | 0.41 | 91.5 | 0.19 | 1650 | 1.12 | 48.5 | 26.6 | 4.83 | 155 | nm |
| PW;2014 4200 | 18.4 | 87.5 | 2.84 | 1630 | 1.2 | 31.8 | 0.027 | 158 | 155.4 | 80.5 |
| PW; 2014 4240 | 0.48 | 47.3 | 0.226 | 1290 | 1.12 | 30 | 0.01 | 108 | 138.3 | 94.3 |
| IW;2001; 4200[a] | 7 | 74 | 1.4 | 1900 | 1.8 | 34 | nm | 180 | 167 | 140 |
| PW;2011; well head[b] | 0.07–0.8[c] | 68–89 | 0.1–2.2 | 1170–1340 | 1.07–1.16 | 41–88 | 0.01–0.7 | 233–123 | 140–152 | 24–37 |

[a] Data from Regenspurg et al. (2010).
[b] Range from long term circulation (in August, September 2011) of each about 10 samples collected at wellhead at 53–100 °C (Feldbusch et al., 2013).
[c] Two outliers were detected in this sequence: one sample showed a Cu concentration of 2 and one of 97.7 mg/L (data not included in the range).

copper: 8.9 g/cm$^3$). This also explains, why the proportion of barite is less (15–25 wt%) in the borehole fill whereas the filter residue and CT samples contained more than 50% of barite (Fig. 7).

### 4.2. Formation of laurionite

Laurionite appears to be the predominant Pb phase in the precipitates as identified by XRD and SEM (Figs. 5 and 6). In other environments, laurionite is typically a product of industrial operations; e.g. landfill leaching in soils, or oxidation of Pb ore deposits (Ioannidis et al., 2006). It was also found in scales of a geothermal field in Kamchatka (Povarov et al., 2003) and of gas wells in NW Europe (Schmidt, 1998). Its temperature-dependent precipitation requires high Pb and chloride concentrations as well as neutral to high pH-values (Mann and Deutscher, 1980). According to equation (Eq. (1)) laurionite formation releases protons thus explaining the strong control of the pH value for laurionite saturation that was calculated by PhreeqC for 20 and 150 °C (Fig. 10b). The released acid must, however, immediately be consumed in the GrSk well due to around neutral pH values of the fluid (Table 5). For neutralization either acid steel corrosion (Eq. (2)) or calcite dissolution (Eq. (3)) can be considered, i.e.:

$$Pb^{2+} + 2Cl^- + 2H_2O \rightarrow PbOHCl + H_3O^+ + Cl^- \quad (1)$$

$$Fe_0 + 2H_3O^+ + 2Cl^- \rightarrow Fe^{2+} + 2H_2O + H_2 + 2Cl^- \quad (2)$$

$$CaCO_3 + 2H_3O^+ \rightarrow Ca^{2+} + CO_2 + 3H_2O \quad (3)$$

Calcite, a known pH-buffer e.g. for neutralizing mine tailings (Jurjovec et al., 2002), occurs at the GrSk site both, as minor component in the precipitate samples (Fig. 7) and as accessory mineral in the reservoir rocks (Trautwein, 2005). In contrast to Cu and $BaSO_4$, the Pb content in of the precipitates decreased with increasing depth along the profile of CO-cf samples (Fig. 8). Although the CT operation strongly disturbed the sediment column at the upper ~100 m of the fill profile (until 4212 m, Reinsch et al., in press), the very low Pb content below 4280 m depth indicates that conditions in the well at larger depth (or higher age) did not favor precipitation of laurionite and other Pb phases (Fig. 8). Since the pH is the dominant factor controlling laurionite precipitation, it is most likely that the pH value increased over time in the borehole for example due to alternating contributions of inflowing reservoir fluid or due to destruction of the cementation of the borehole completion behind the liner that could have released hydroxide ions. The latter assumption of local pH increase due to dissolving cementation would also explain why the formation of laurionite occurred apparently not from the beginning of well operation but later, when already some sediment had filled the well (Fig. 8).

### 4.3. Formation of elemental copper and iron oxide

Native copper represents with about 50 wt% the dominant solid component of the bailer samples (Table 3, Fig. 7). These are considered as rather autochthonous because due to its high density only the smaller $Cu^0$ particles can be transported to the surface by flushing or pumping resulting in decreased Cu content in CT and FR samples and to a lesser degree also in the CO samples. Dissolved Cu concentrations measured both in deep fluid and in above ground sampled fluid was typically relatively low and even decreased over time from 0.11 mM (2001) to 0.001–0.006 mM (2013; Table 5). We assume that dissolved Cu (as Cu(I) or Cu(II)) is reduced to solid $Cu^0$ when the fluid enters the borehole by oxidation of $Fe^0$ (the main component of the carbon steel liner material). This reaction is likely to happen due to the large differences in standard state

redox potentials ($E_0$) for the two half reactions (Eq. (4a) or (4b) compared to (4c)):

$$Cu^{2+} + 2e^- \rightarrow Cu^0 \quad E_0 = 0.34\,V \tag{4a}$$

$$Cu^{+} + e^- \rightarrow Cu^0 \quad E_0 = 0.52\,V \tag{4b}$$

$$Fe^0 \rightarrow Fe^{2+} + 2e^- \quad E_0 = -0.44\,V \tag{4c}$$

The calculation of the equilibrium constant from the standard state potentials ((4a) and (4c)) for the redox reaction:

$$Cu^{2+} + Fe^0 = Fe^{2+} + Cu^0 \tag{4d}$$

gives a log $K$ of 25.17 = $[Fe^{2+}]/[Cu^{2+}]$ for standard conditions. Since the measured Fe concentrations are significantly higher than Cu concentrations the reaction seems indeed to proceed in the suggested direction.

The high Cu content of precipitates indicates that the Cu concentration of the reservoir fluid must be much higher than the concentrations normally measured in the fluid (<0.5 mg/L; Table 5). It is known that heavy metal concentrations can be enormously increased in highly saline brines by formation of metal chloride complexes (e.g. $CuCl_2$, $CuCl_3^-$, $CuCl^+$) as calculated by PhreeqC or according to Wells (1984). Upon entering the borehole, the dissolved Cu would be instantly removed from the solution by reduction to $Cu^0$ and precipitation. An indication for higher Cu concentration in the undisturbed reservoir fluid was obtained by measuring Cu in two deep fluid samples (4200 m and 4240 m) collected after the production lift test following the wellbore cleanout. The Cu content of the sample collected at 4200 m was indeed very high (18 mg/L; Table 5), but still not did not necessarily represent the "real" Cu concentration of the reservoir fluid. The reduction of the Cu(I)- and Cu(II)-complexes presumably also happens on the reservoir site of the liner within close proximity of the well provided that the steel is in contact with the Cu thus allowing an electron transfer between the two redox partners. The amount of Cu precipitation in the borehole would contribute to the fill at the well bottom, whereas another unknown amount of native copper might be enriched at the outer (reservoir) side of the liner growing into the pores of the reservoir thus causing a formation damage (clogging of the pores) that could be responsible for observed decreasing productivity of the well.

Iron, the redox partner for Cu, could be oxidized from Fe(0) to Fe(II) or Fe(III). Precipitation of secondary Fe minerals can be assumed since the Fe concentration in the fluid did not increase over time (Table 5). Analysis by XRD, magnetic susceptibility, and Mössbauer spectroscopy confirmed the presence of several solid Fe compounds with magnetite as the most dominant mineral. Most likely magnetite forms initially out of an amorphous Fe(II) phase such as green-rust (e.g. $Fe(OH)_2$) or Fe–$SiO_4$ as both measured using Mössbauer spectroscopy on samples kept under anoxic conditions. Previous studies have identified $Fe(OH)_2$ as product of steel corrosion in saline solutions (Nagies and Heusler, 1997). It could also form directly by the oxidation of steel and simultaneous reduction of water to hydrogen ($H_2$) under reducing conditions (Schon and Heidendael, 1996):

$$Fe_0 + 2H_2O \rightarrow Fe(OH)_2 + H_2 \tag{5}$$

Confirmation for this reaction happening at the GrSk production well was obtained by measuring the gas composition over time of fluid circulation tests at the release of the gas separator. Hydrogen content ranged between 0.2 and 20 vol% with highest $H_2$ concentrations released during shut-in periods (Regenspurg et al., 2013). A weak sextet in the Mössbauer spectra of bailer sample B116 (Table 4) indicated an Fe(II) phase, which is consistent with green rust minerals measured at low temperature (140 K and 77 K; Cuttler et al., 1990). Green rusts are metastable iron phases that transform to more stable minerals such as the mixed valence Fe(II)/Fe(III) oxide magnetite (Cornell and Schwertmann, 1996). Magnetite formation by further oxidation of the $Fe(OH)_2$ in hot, saline solutions has been described by Schikorr (1929a,b):

$$3Fe(OH)_2 \rightarrow Fe_3O_4 + 2H_2O + H_2 \tag{6}$$

This reaction can happen at high salinities in the observed temperature range (Nagies and Heusler, 1997). Furthermore, $Fe(OH)_2$ can react with atmospheric $O_2$ during sample storage or by $O_2$ dissolved in the drilling fluid used for the clean out operation:

$$3Fe(OH)_2 + ½O_2 \rightarrow Fe_3O_4 + 3H_2O. \tag{7}$$

Some additional, Mössbauer spectra indicated the formation of a poorly crystalline Fe(III) hydroxide such as ferrihydrite (Fig. 9) which signifies fast Fe(II) oxidation for example due to contact of the scaling material with atmospheric oxygen.

Evidence for liner corrosion was further given by caliper measurements. The observed increase of metal loss with increasing well depth indicates that corrosion predominantly occurs at the bottom of the well, where fluid is entering the borehole, and gradually diminishes toward shallower depths.

### 4.4. Origin and mobility of Cu and Pb in the geothermal fluid

The concentrations of many heavy metals in the Groß Schönebeck fluid are relatively high with, for example, up to 233 mg Pb and 105 mg Zn (Table 5). Similarly, the Cu concentration was assumed to be much higher in the reservoir fluid as measured in the sampled fluid. From these observations the question of the origin of these high concentrations of metals in the reservoir fluid arises.

Deep sedimentary basin fluids such as the Rotliegend brines are known for their complex composition and very high salinity (e.g. Hanor, 1994; Kharaka and Hanor, 2004). The sedimentary environment of the Middle European Permian Rotliegend basin was a semiarid stream and river delta landscape where water evaporated in salt pans and sand and gravel deposited above andesitic and rhyolithic rocks (Pietranik et al., 2013) eventually forming the red clastic sediment layer of mainly sand-, silt- and mudstone (McCann, 1998a,b). The end of this geologic period (begin Zechstein) is marked in the stratigraphic profile by a thin, bituminous marl or shale that formed after rapid marine transgression in an anoxic deep sea environment (Vaughan et al., 1989; Borg et al., 2012). This "Kupferschiefer" formation often contains minable Cu deposits along with Pb and Zn which have been widely exploited over the last centuries (Kopp et al., 2008). The copper belt stretches around central Europe forming the boundary between evaporates of the Zechstein and the red beds of the Rotliegend (Vaughan et al., 1989; Borg et al., 2012). It was also encountered at the GrSk site with a thickness of 0.4 m at 3894 m (measured depth, Fig. 1; Moeck et al., 2005) and a Cu content, as measured in drill cuttings, of about 900 ppm (unpublished data). The formation of the *Kupferschiefer* is discussed for several central European sedimentary basins such as the Thuringian or the Polish Basin (Hitzmann et al., 2010; Kopp et al., 2008; Blundell et al., 2003). The reducing conditions at the bottom of the deep sea allowed bacterial sulfate reduction thus producing hydrogen sulphide which would react with heavy metals forming poorly soluble sulphide ores such as chalcosine ($Cu_2S$), galena (PbS) or sphalerite (ZnS) (Borg et al., 2012). The sources of Cu and Pb are generally assumed to be the Autunian volcanic rocks that underlie the Rotliegend sandstones (Hitzmann et al., 2010; Borg et al., 2012; Geißler et al., 2008), which contain 10–270 ppm, locally even up to 0.6 wt% Cu (Blundell et al., 2003). Copper and Pb concentrations of reservoir rocks (cuttings) from the GrSk site correlate and are in the same range in volcanic -and sedimentary rocks (12–146 ppm Cu and 20–97 ppm Pb, respectively; Regenspurg et al.,

2014). Basin-wide mobilization of mineralizing fluids occurred due to major tectonic events attributed to the break-up of Pangea and extensional faulting during the closure of the Tethyan Ocean in later geologic times (late Jurassic to mid-Cretaceous, and Tertiary, resp.; Borg et al., 2012). Thereby, saline Rotliegend fluids migrated along fractures into the volcanic rocks leaching and mobilizing the heavy metals through the formation of highly soluble chloride complexes (Blundell et al., 2003; Hitzmann et al., 2010). Due to this strong complexation, several hundred ppm of these heavy metals could theoretically occur in the Rotliegend formation fluids. However, measurements of the true Cu concentration are very difficult to determine due to the above discussed redox reactions that likely occur during sampling. Several studies estimate via mass balances and model assumptions respectively Rotliegend fluid Cu concentrations of between 60 ppm (Blundell et al., 2003), 127 ppm (Cathles et al., 1993), and 1000 ppm (Jowett, 1986).

Whilst high Cu concentrations appear to be a very typical phenomenon for fluids of the Rotliegend sandstones, increased Pb and Ba concentrations are known from many brines of geothermal sites in Germany and elsewhere (Lüders et al., 2010; Schreiber et al., 2012). They are currently under investigation due to their association with increased amounts of naturally occurring radioactive materials (e.g. $^{226}$Ra, $^{228}$Ra, and $^{210}$Pb; Degering and Kohler, 2011). For the Permian Rotliegend fluid, the origin of Pb is, due to mentioned correlation with Cu, most probably also the volcanic rock where Pb is originally incorporated in feldspars (Borg et al., 2012).

## 5. Conclusion

This study explains the relevant processes responsible for the scaling and corrosion observed in the production well at the Groß Schönebeck geothermal site. They can be attributed to the geological setting, interaction of the fluid with the wellbore completion, and operational conditions. Due to its origin from Rotliegend rocks, the geothermal fluid produced at the site is enriched in Ba, Pb, and Cu that mainly precipitated in the production well as barite, laurionite, native copper, and magnetite due to the following processes: (I) Barite precipitates during cooling of the fluid mainly at shut-in periods. (II) Laurionite forms upon pH increase or temperature decrease. Its precipitation releases acid that is most likely consumed by calcite dissolution, steel corrosion, or by reaction with the corroding cementation behind the liner thus buffering the pH value to around neutral. (III) The redox reaction between dissolved Cu and the steel liner occurs immediately upon contact with the fluid resulting in the formation of magnetite and native copper.

Especially the high Cu concentration of Rotliegend formation fluids represents a severe problem for wells with carbon steel completion. This problem seems not obvious since the Cu concentration is typically underestimated because dissolved Cu would likely react with the casing or sampling tool thus precipitating and removing Cu before sampling.

In general, the frequent changes of fluid production (supply of fresh fluid with potentially precipitating compounds) and shut-in periods (cooling) accelerated mineral precipitation. To prevent the formation of barite and laurionite downhole, a constant and strong fluid production must be ensured to increase temperature and thus keep these minerals under saturated. Laurionite precipitation could be prevented by adjusting the pH value to pH < 7. Above ground the application of scale inhibitors should be considered to prevent barite formation at the heat exchanger. In order to avoid the redox reaction between Cu and Fe, inert or highly alloyed materials have to be applied in the fluid loop.

Apart from operational implications, the high Cu content found in this study confirms assumptions from literature suggesting that Cu originates from Autunian volcanic rocks leached out by saline Rotliegend formation fluids (e.g. Hitzmann et al., 2010; Borg et al., 2012). This offers an important contribution within the field of economic geology by indicating high Cu concentration in Rotliegend formation fluids, which might even be of minable value.

## Acknowledgements

The authors kindly acknowledge Sabine Rauschenberg (Technical University Berlin), the VKTA Rossendorf for analytical measurements, Birgit Plessen and Petra Meier for TIC and TOC analysis, and Ilona Schäpan for assistance with the scanning electron microscope. X-ray fluorescence spectroscopy was performed at the department of Material Science and Physics, at the University of Salzburg. Thanks also to Carolin Zorn for numerous sample preparations and microscopic analysis. For technical support during field works at the GrSk site we thank Claudia Tamara Rach, Andreas Kratz, Thomas Becker and all people of the department 4.1 that were involved. For financial support we thank the Federal Ministry of Environment, Nature Conversation and Nuclear Safety (BMU) and the Federal Ministry of Education and Research (BMBF).

## Appendix A. Supplementary data

Supplementary data associated with this article can be found, in the online version, at doi:10.1016/j.geothermics.2015.01.003.

## References

Altmaier, M., Metz, V., Neck, V., Müller, R., Fanghänel, T.H., 2003. Solid–liquid equilibria of $Mg(OH)_2$(cr) and $Mg_2(OH)_3Cl_4H_2O$(cr) in the system Mg–Na–H–OH–Cl–$H_2O$ at 25 °C. Geochim. Cosmochim. Acta 67 (19), 3595–3601.

Bancroft, G.M., Maddock, A.G., Burns, R.G., 1967. Applications of the Mössbauer effect to silicate mineralogy—I. Iron silicates of known crystal structure. Geochim. Cosmochim. Acta 31, 2219–2246.

Bin Merdhah, A.B., Yassin, A.A.M., 2007. Barium sulfate scale formation in oil reservoir during water injection at high barium formation water. J. Appl. Sci. 7, 2393–2403.

Blount, C.W., 1977. Barite solubilities and thermodynamic quantities up to 300 °C and 1400 bar. Am. Miner. 62, 942–957.

Blundell, D.J., Karnkowski, P.H., Alderton, D.H.M., Oszczepalski, S., Kucha, H., 2003. Copper mineralization of the Polish Kupferschiefer: a proposed basement fault–fracture system of fluid flow. Econ. Geol. 97 (7), 1487–1495.

Borg, G., Piestrzynski, A., Bachmann, G.H., Püttmann, W., Walther, S., Fiedler, M., 2012. An overview of the European Kupferschiefer deposits. Soc. Econ. Geol. 16, 455–486.

Cathles, I.L.M., Oszczepalski, S., Jowett, E.C., 1993. Mass balance evaluation of the late diagenetic hypothesis for Kupferschiefer Cu mineralization in the Lubin basin of southwestern Poland. Econ. Geol. 88, 948–956.

Collins, I.R., 2005. Predicting the location of barium sulfate scale formation in production systems. In: Society of Petroleum Engineers International Symposium on Oilfield Scale, Conference Paper, 94366 – MS, Aberdeen, UK.

Cornell, C., Schwertmann, U., 1996. The Iron Oxides. VCH Weinheim, Weinheim.

Cuttler, A.H., Man, V., Cranshaw, T.E., Longworth, G., 1990. A Mössbauer study of green rust precipitates: I. Preparations from sulphate solutions. Clay Miner. 25 (3), 289–301.

Degering, D., Kohler, M., 2011. Gamma-spectrometric analysis of high salinity fluids – how to analyze radionuclides of the thorium decay chain far from radioactive equilibrium? Appl. Radiat. Isot. 69 (11), 1613–1617.

Dennis, B., 1990. Casing corrosion evaluation using wireline techniques. J. Can. Pet. Technol. 29 (4), 100–112.

Feldbusch, E., Regenspurg, S., Banks, J., Milsch, H., Saadat, A., 2013. Alteration of fluid properties during the initial operation of a geothermal plant – results from in situ measurements in Groß Schönebeck. Environ. Earth Sci., 1–12.

Frick, S., Regenspurg, S., Kranz, S., Milsch, H., Saadat, A., Francke, H., Brandt, W., Huenges, E., 2011. Geochemical and process engineering challenges for geothermal power generation. Chem. Ingen. Tech. 83 (12), 2091–2104.

Geißler, M., Breitkreuz, C., Kiersnowski, H., 2008. Late Paleozoic volcanism in the central part of the Southern Permian Basin (NE Germany, W Poland): facies distribution and volcano-topographic hiati. Int. J. Earth Sci. (Geol. Rundsch.) 97, 973–989.

Hanor, J.S., 1994. Origin of saline fluids in sedimentary basins. In: Parnell, J. (Ed.), Geofluids: Origin, Migration and Evolution of Fluids in Sedimentary Basins, vol. 78. Geological Society Special Publication, pp. 151–174.

Henninges, J., Brandt, W., Erbas, K., Moeck, I., Saadat, A., Reinsch, T., Zimmermann, G., 2012. Downhole monitoring during hydraulic experiments at the in-situ geothermal lab Gross Schönebeck. In: 37th Workshop on Geothermal Reservoir Engineering, Stanford, USA, pp. 51–56.

Hitzmann, M.W., Selley, D., Bul, S., 2010. Formation of sedimentary rock-hosted stratiform copper deposits through earth history. Econ. Geol. 105, 627–639.

Huenges, E., Trautwein, U., Legarth, B., Zimmermann, G., 2006. Fluid pressure variation in a sedimentary geothermal reservoir in the North German Basin: case study Groß Schönebeck. Pure Appl. Geophys. 163 (10), 1–12.
Huenges, E. (Ed.), 2010. Geothermal Energy Systems: Exploration, Development and Utilization. Wiley-VCH, Weinheim, 463 pp.
Ioannidis, Th.A., Zouboulis, A.L., Matis, K.A., 2006. Effective treatment and recovery of laurionite-type lead from toxic industrial solid wastes. Sep. Purif. Technol. 48 (1), 50–56.
Johnson, J.W., Oelkers, E., Helgeson, H., 1992. SUPCRT92: a software package for calculating the standard molal thermodynamic properties of minerals, gases, aqueous species, and reactions from 1 to 5000 bar and 0 to 1000 °C. Comput. Geosci. 19, 899–947.
Jowett, E.C., 1986. Genesis of Kupferschiefer Cu–Ag deposits by convective flow of Rotliegend brines during Triassic rifting. Econ. Geol. 81, 1823–1837.
Jurjovec, J., Ptacek, C.J., Blowes, D.W., 2002. Acid neutralization mechanisms and metal release in mine tailings: a laboratory column experiment. Geochim. Cosmochim. Acta 66 (9), 1511–1523.
Kharaka, Y.K., Hanor, J.S., 2004. Deep fluids in the continents: I: Sedimentary rocks. In: Drever, J.L., Holland, H.F., Turekian, K.K. (Eds.), Treatise on Geochemistry. Surface and Groundwater, Weathering, and Soils, vol. 5, pp. 499–540.
Kharaka, Y.K., Maest, A.S., Carothers, W.W., Law, L.M., Lamothe, P.J., Fries, T.L., 1987. Geochemistry of metal-rich brines from central Mississippi Slat Dome Basin, USA. Appl. Geochem. 2, 543–561.
Kehrer, P., Orzol, J., Jung, R., Jatho, R., Junker, R., 2007. The GeneSys project – a contribution of Geozentrum Hannover to the development of Enhanced Geothermal Systems (EGS). Z. Dtsch. Ges. Geowiss. 158 (1), 119–132.
Kopp, J., Hermann, S., Höding, T., Andreas, S., 2008. Enrichments of non-ferrous metals at the Zechstein-base between Spremberg and Weißwasser. Z. Geol. Wiss. 36 (1), 75–114.
Li, Y., Ma, Y., 2009. Corrosion of low carbon steel in atmospheric environments of different chloride content. Corros. Sci. 51 (5), 997–1006.
Lüders, V., Plessen, B., Romer, R.L., Weise, S.M., Banks, D.A., Hoth, P., Dulski, P., Schettler, G., 2010. Chemistry and isotopic composition of Rotliegend and Upper Carboniferous formation waters from the North German Basin. Chem. Geol. 276 (3–4), 198–208.
Mann, A.W., Deutscher, R.L., 1980. Solution geochemistry of lead and zinc in water containing carbonate, sulphate and chloride ions. Chem. Geol. 1–4, 293–311.
McCann, T., 1998a. Sandstone composition and provenance of the Rotliegend of the NE German Basin. Sediment. Geol. 116, 177–198.
McCann, T., 1998b. The Rotliegend of the NE German Basin: background and prospectivity. Pet. Geosci. 4, 17–27.
McLin, K.S., Moore, J.N., Hulen, J., Bowman, J.R., Berard, B., 2006. Mineral characterization of scale deposits in injection wells; Cosco and Salton Sea geothermal fields. In: Proceedings, Thirty-First Workshop on Geothermal Reservoir Engineering, Stanford, California.
Moeck, I., Brandt, W., Schulz, A., 2005. Geologisch – technischer Abschlussbericht der Bohrung Gt Groß Schönebeck 4/05., pp. 56 p.
Monnin, C., Galinier, C., 1998. A thermodynamic model for the solubility of barite and celestite in electrolyte solutions and seawater to 200 °C and to 1 kbar. Chem. Geol. 153, 187–209.
Monnin, C., Galinier, C., 1988. The solubility of celestite and barite in electrolyte solutions and natural waters at 25 °C: a thermodynamic study. Chem. Geol. 71, 283–296.
Moog, H.C., Cannepin, R., (GRS-A-3749) 2014. Entwicklung von thermodynamischen Daten für die Belange der thermodynamischen Gleichgewichtsmodellierung von Prozessen in tiefen, geothermalen Schichten. In: Teilprojekt A (GRS): Bestimmung von Ionenwechselwirkungskoeffizienten und Aufstellung eines Reservoirmodells., ISBN 978-3-944161-17-4, pp. 165 p.
Murad, E., 2010. Mössbauer spectroscopy of clays, soils and their mineral constituents. Clay Miner. 45, 413–430.
Murad, E., Cashion, J., 1980. The Mössbauer spectrum of ferrihydrite and its relations to those with other ion oxides. Am. Miner. 65, 1044–1049.
Nagies, F., Heusler, K.E., 1997. Corrosion of metallic materials in hot salt brines. Electrochim. Acta 43 (1–2), 41–51.
Parkhurst, D.L., Appelo, C.A.J., 2011. User's guide to PhreeqC – a computer program for speciation, reaction path, 1D-transport and inverse geochemical calculation. In: U.S. Geological Survey Water-Resources Investigations Report 99-4259.
Pietranik, A., Słodczyk, E., Hawkesworth, C.J., Breitkreuz, C., Storey, C.D., Whitehouse, M., Milke, R., 2013. Heterogeneous zircon cargo in voluminous late Paleozoic Rhyolites: Hf, O isotope and Zr/Hf records of plutonic to volcanic magma evolution. J. Pet. (First published online: April 23).
Pitzer, K.S., Mayorga, G., 1973. Thermodynamics of electrolytes. II. Activity and osmotic coefficients for strong electrolytes with one or both ions univalent. J. Phys. Chem. 77 (19), 2300–2308.
Povarov, O., Saakyan, V., Nikolski, A., Luzin, V., Tomarov, G., Sapozhnikov, M., 2003. Experience of creation and operation of geothermal power plants at Mutnovsky geothermal field, Kamchatka, Russia. In: International Geothermal Conference, Sept. 2003, Reykjavík, Session #1.
Rancourt, D.G., Ping, J.Y., 1991. Voigt-based methods for arbitrary-shape static hyperfine parameter distributions in Mössbauer spectroscopy. Nucl. Instrum. Meth. Phys. Res. B: Beam Interact. Mater Atoms 58, 85–97.
Regenspurg, S., Wiersberg, T., Brandt, W., Huenges, E., Saadat, A., Schmidt, K., Zimmermann, G., 2010. Geochemical properties of saline geothermal fluids from the in-situ geothermal laboratory Groß Schönebeck (Germany). Chemie der Erde 70 (Suppl. 3), 3–12.
Regenspurg, S., Feldbusch, E., Saadat, A., 2013. Corrosion processes at the geothermal site Groß Schönebeck (North German Basin). In: Conference Proceeding, NACE 2013, Orlando, Florida.
Regenspurg, S., Dilling, J., Mielcarek, J., Korte, F., Schkade, U.-K., 2014. Naturally occurring radionuclides and their geochemical interactions at a geothermal site in the North German Basin. Environ. Earth Sci. (Online First).
Reinsch, T., Regenspurg, S., Feldbusch, E., Saadat, A., Huenges, E., Erbas, K., Zimmermann, G., Henninges, J., Pfeil, S., 2015. Reverse clean-out in a geothermal well: analysis of a failed coiled tubing operation. SPE Prod. Oper., http://dx.doi.org/10.2118/174080-PA (in press).
Sandia National Laboratories, 2007. In-Drift Precipitates/Salts Model EQ3/6 Pitzer Datenbank ANL-EBS-MD-000045 REV 03.
Schikorr, G., 1929a. Über das System Eisen-Wasser. Z. Elektrochem. 55 (2), 62–65.
Schikorr, G., 1929b. Über die Reaktion zwischen Eisen, seinen Hydroxyden und Wasser. Z. Elektrochem. 55 (2), 65–70.
Schon, T., Heidendael, M., 1996. Wasserstoffbildung durch Metallkorrosion. Berichte des Forschungszentrums Jülich (Jül-3495, ISSN 0944-2952).
Schreiber, J., Nitschke, F., Seibt, A., Genter, A., 2012. Geochemical and mineralogical monitoring of the geothermal power plant I Soultz-Sous-Forets (France). In: Proceedings Thirty-Seventh Workshop on Geothermal Reservoir Engineering Stanford University, Stanford, California.
Schmidt, A.P., 1998. Lead precipitates from natural gas production installations. J. Geochem. Explor. 62 (1–3), 193–200.
Seibt, P., Kabus, F., Hoth, P., 2005. The Neustadt-Glewe geothermal power plant – practical experience in the reinjection of cooled thermal waters into sandstone aquifers. In: Proceedings World Geothermal Congress 2005, 24–29 April, Antalya, Turkey.
Sharma, P., Ofner, J., Kappler, A., 2010. Formation of binary and ternary colloids and dissolved complexes of organic matter, Fe and As. Environ. Sci. Technol. 44, 4479–4485.
Shen, D., Fu, G., AlSaiari, H., Kan, A.T., Tomson, M.B., 2009. Barite dissolution/precipitation kinetics in porous media and in the presence and absence of a common scale inhibitor. Soc. Pet. Eng. J., 462–471.
Trautwein, U., (Ph.D. thesis) 2005. Poroelastische Verformung und petrophysikalischeEigenschaften von Rotliegend Sandsteinen. Technical University of Berlin.
Vaughan, D.J., Sweeney, M.A., Friedrich, G., Diedel, R., Haranczyk, C., 1989. The Kupferschiefer: an overview with an appraisal of the different types of mineralization. Econ. Geol. 84, 1003–1027.
Wells, A.F., 1984. Structural Inorganic Chemistry, 5th ed. Oxford University Press, Oxford, UK.
Wolfgramm, M., Seibt, A., Hurter, S., Zimmermann, G., 2003. Origin of geothermal fluids of Permo-Carboniferous rocks in the NE German Basin (NE Germany). J. Geochem. Explor. 78–79, 127–131.
Wolery, T., 1992. Eq3/6, a software package for geochemical modeling of aqueous systems: Package overview and installation guide (version 7.0) ucrl-ma-110662. Technical Report. Lawrence Livermore National Laboratory, Livermore.
Zimmermann, G., Moeck, I., Blöcher, G., 2010. Cyclic waterfrac stimulation to develop enhanced Geothermal System (EGS) – conceptual design and experimental results. Geothermics 39, 56–69.
Zimmermann, G., Reinicke, A., 2010. Hydraulic stimulation of a deep sandstone reservoir to develop an Enhanced Geothermal System: laboratory and field experiments. Geothermics 39, 70–77.